GKSS
FORSCHUNGSZENTRUM
in der HELMHOLTZ-GEMEINSCHAFT

Final Draft
of the original manuscript:

Mueller, B.; Pfrunder, F.; Chiocca, L.; Ruse, N.D.; Beckmann, F.:
Visualizing the complex morphology of fatigue cracks in voxel-based 3D datasets
In: Materials Science and Technology (2006) Maney

DOI: 10.1179/174328406X114162

Visualizing the complex morphology of fatigue cracks in voxel-based 3D datasets

Bert Müller* (bmueller@vision.ee.ethz.ch)
Felix Pfrunder (felix.pfrunder@fss-group.com)
Loris Chiocca (loris@chiocca.ch)
Computer Vision Laboratory, ETH Zurich, Sternwartstr. 7, 8092 Zürich, Switzerland,
N. Dorin Ruse (dorin@interchange.ubc.ca)
Faculty of Dentistry, University of British Columbia, Vancouver, Canada V6T 1Z3
Felix Beckmann (felix.beckmann@gkss.de)
GKSS-Research Center, 21502 Geesthacht, Germany

Abstract: Fatigue cracks are usually characterized by surface sensitive techniques after specimen failure. High-resolution micro computed tomography (μCT) based on synchrotron radiation allows the non-destructive visualization of crack morphology and evaluation of fatigue crack formation/propagation before specimen failure. The visualization of the complex fracture morphology with characteristic features out of the acquired set of slices is, however, challenging. To obtain a reasonable estimate, two approaches are generally used: the determination of mass centre points in the hollow space and the minimum intensity search in parallel projections. The more sophisticated approach using the elastically deformable contour model, the physical analogy of a rubber band, termed snakes, gives rise to crack morphologies with much less artefacts. The approach was used in this study for the characterization of fatigue cracks in poly(methylmethacrylate) (PMMA) and a dental ceramic. The search for the appropriate snake parameters works much better for homogeneous materials, here PMMA, than for inhomogeneous materials, here a dental ceramic. For the ceramic, the regions where the snakes approach provided reasonable results were restricted. Combining μCT with sophisticated computer vision techniques enables the unique characterization of cracks at the micrometer scale.

Keywords: micro-tomography, fatigue crack, crack morphology, elastically deformable contour model

*Corresponding author, phone +41 44 63 36190, Fax +41 44 63 21199

Introduction

The remodelling process present in some hard tissues, such as bone, can repair micro-cracks. Since such a process has not yet been implemented in biomaterials, the study and characterization of fatigue micro-cracks could play an important role in their life prediction. Micro computed tomography (μCT) is a non-destructive, 3D method of micrometer resolution that could greatly facilitate such studies. The analysis of the huge 3D data sets generated by μCT, usually of gigabyte size, cannot be performed using commercially available software but needs the development and implementation of sophisticated algorithms. Combining high-resolution μCT with sophisticated image analysis could allow the accurate determination of crack length to enable the accurate determination of the rate of crack propagation and therefore the accurate determination of the fatigue behaviour of the material to be optimized. Such measurements should also provide the crack morphology with isotropic spatial and density resolution in the three orthogonal directions, which can be used in the investigation of the failure mechanism. Therefore, these rather time-consuming precision measurements could be used to validate and/or calibrate other less sophisticated methods currently used for the crack length determination and the non-destructive morphology characterization.

The first problem to be mastered is the detection of the cracks in the tomogram. Using the absorption contrast mode, the crack has to be thick enough to significantly reduce the absorption in the related voxels.[1] Inhomogeneity of the material, all kinds of artefacts, and the noise in the tomogram complicate the crack detection. To segment the cracks, an appropriate threshold for the region of interest has to be chosen, although a certain tolerance exits.[2]

Even if the first problem is mastered, the crack has to be visualized on the basis of the tomogram, which could be especially difficult for the composite-type materials used in dentistry. In the simple 2D slices, the crack might be detectable but its 3D morphology is hardly seen, if just state-of-the-art volume rendering is applied.[3] An algorithm is required, which detects the coordinates of all voxels belonging to the crack. Because of artefacts and noise, however, many voxels, which are outside the crack, exhibit the same local absorption but have to be eliminated. More important, often only a part of the crack is identified, since the crack can be closed in certain regions.[3] Therefore, we propose to use the active contour model,[4] which is based on a physical analogy: the energy of a rubber band, termed “snake”, with certain properties is minimized adjusting the 1D band line-wise to the detected crack voxels. This approach needs the identification of the appropriate snake parameters, which finally allow for convergence.[5]

Materials and methods

Notch-less triangular prism fracture toughness tests

Fracture toughness tests belong to the standard engineering procedures to characterize dedicated materials. Different testing and specimen designs have been introduced to determine the fracture toughness of dental materials including calcium hydroxide preparations,[6] denture base acrylic resins,[7] dental ceramics[8] and composites,[9] cements and various adhesive interfaces.[10] These studies have also incorporated the effect of the environment, thermal cycling, and cyclic fatigue on the fracture toughness.

The chevron-notched short rod (CNSR) configuration introduced by Barker[11] and modified by Pilliar[12,13] is especially suited for fracture toughness tests of brittle materials. The test involves a relatively small sample prepared by cutting a chevron notch in a cylindrical specimen. This process is cumbersome and difficult to control, especially with small samples of very brittle materials such as dental ceramics. It is even more complex and prone to error when used to characterize bonded interfaces. Therefore, the notch-less triangular prism fracture toughness test has been developed and validated through finite element analysis.[14] The objective was to retain the overall geometry of the CNSR but to avoid the cumbersome notching procedure. This procedure simply uses the notch-less triangular prism specimen, which is fixed in the holder to achieve the CNSR configuration.

A sharp blade helps to create an about 0.1 mm deep crack initiation point midway along one of the prism edges. The test assembly, prism and holder, is secured in the custom designed grips and attached to the computerized universal testing machine (Instron model 4301, Instron Canada Inc.). An extensometer is attached between the lips of the grips. The assembly is loaded in tension at a crosshead speed of 0.1 mm/min, and the load and the displacement are constantly monitored and recorded. Hence, well-defined conditions to introduce fatigue cracks into the prism are realized.

If the prism is transparent, optical techniques can be used to follow the crack formation. If, however, the specimen is opaque, the crack formed can only be made visible after specimen failure. Fig. 1 shows photographic and SEM images of fatigue fractured surfaces in a failed specimen. The initiation point and characteristic rough and flat areas are visible.

Synchrotron-radiation-based micro computed tomography

Synchrotron-radiation-based μCT (SRμCT) in absorption contrast mode is well established to quantitatively characterize the 3D structure of different kinds of materials and the anatomy of

various human tissues with true micrometer resolution. The main advantage with respect to conventional μCT is the much higher photon flux, which offers to eliminate all photons but the ones of desired energy, and still maintain a reasonable period of time for data acquisition. Bragg reflection by single crystals permits the realization of a tuneable x-ray source. Because the x-ray absorption coefficient μ strongly depends on both energy E and atomic number Z, the choice of the photon energy can be optimized minimizing the total exposure time at any prescribed sensitivity by the relation $\mu(E,Z) \cdot D = 2$, where D corresponds to the average sample diameter, as shown by Grodzins.[15] Therefore, for the present study we selected photon energies of 11 keV and 24 keV for the investigation of PMMA and ceramic specimens, respectively. The spatial resolution was determined by the modulation transfer function of an edge of a gold plate recorded under the conditions applied for the data acquisition[16] and corresponds to 8.0 μm and 5.2 μm for the PMMA and ceramic specimen, respectively. Note that the voxel lengths were chosen to 5.0 μm and 3.3 μm because of the different specimen cross-sections.

The experiments were carried out at the beamline BW 2 (HASYLAB at DESY) taking advantage of the standard setup for tomography.[17] The fixed exit double crystal monochromator, Si(111) provides the monochromatic x-ray beam of desired energy and necessary flux. The sagitally bent second Si(111) crystal reduces the beam divergence and forms a parallel beam about 10 mm wide and 3 mm high.

This beam is partly absorbed in the sample and generates the projection image on the fluorescence screen (200 μm-thick $CdWO_4$ single crystal). After moderate magnification the image is mapped on a Kodak KAF 1600 CCD-chip (1536 x 1024 pixels, pixel length 9 μm) and acquired using 14 bit digitalization at a frequency of 1.25 MHz. For the present study, 361 projections were recorded by rotating the sample in steps of 0.5° from 0 to 180°. In order to eliminate the beam non-uniformities and account for the detector noise, the difference between the individual bare projections and the dark image was divided by the difference of the beam and the dark image to obtain the corrected projections, which were the basis of the slice by slice reconstruction performed with the filtered back projection algorithm.[18] Nevertheless, image inhomogeneities still existed due to the photon counting statistics and prominent defects in the fluorescence screen.

Results

Selection of the region of interest

The crack started from the crack initiation point and was directly observed at the specimen's surface. This knowledge helped to identify the crack within the voxel-based 3D dataset. Using homogeneous materials, it is rather simple to determine the location of the crack inspecting individual slices, as shown in Fig. 2. Hence, the amount of data for the PMMA specimen with a tomogram size of 1.5 GB could be reduced to 113 MB and for the ceramic specimen with a tomogram size of 2.5 GB to 68 MB, which is a reduction of more than one order of magnitude. The datasets can be even further reduced taking into account the triangular cross section of the specimens used.

Intensity-based segmentation

Intensity-based methods for segmentation belong to the simplest approaches in order to extract details with defined properties out of the 3D dataset. Voxels belonging to the crack should have lower absorption than the surrounding material. If this difference in absorption is high enough on the length scale of resolution, the crack becomes to light. *A priori*, one cannot assume that the product of the width of the crack and the difference in absorption between air and material is sufficient. The data of both PMMA and ceramics clearly demonstrate that even without the use of any contrast agent or preloading the crack is clearly identified.

In order to segment the crack, the threshold for the absorption has to be determined. The tomograms acquired at the beamline BW 2 lead to peaks in the absorption histograms of perfect Gaussian shape.[19] For a two-component system (air – material) two Gaussians accurately describe the histogram as shown in Fig. 3. The slightly higher values between the two peaks are the result of partial volume effects. Because both peaks are well separated, the crossing point of the two Gaussians between grey value 96 and 97, which is not the minimum between both (grey value 98), is the best choice for the threshold.[19] Thus, all voxels with a local absorption represented by grey values up to 96 are set to air, whereby the voxels with a local absorption associated with values beginning from 97 are set to PMMA. This binarization further reduces the size of the dataset and makes easier the identification of the crack. Nevertheless, the thresholding does not allow identifying the crack in a unique manner.

Artefacts and noise in SRμCT

The snake algorithm does not suitable work, if too many ring-like artefacts are present. These artefacts results from defects in the fluorescence screen and give rise to dark or bright spots in the acquired images. They become more numerous during the lifetime of the screen and cannot be fully avoided. Our study was performed at the end of the screen's lifetime and the number of ring-like artefacts was relatively large. Several codes have been developed to process the data with the aim to remove these artefacts replacing the related pixels or voxels by reasonable estimates.[20] The defects in the projections are independent on the rotation angle and thus show up as lines in the sinogram. We have automatically replaced most of these lines averaging the pixels from the left and the right. Although this approach does not remove all artefacts, it considerably reduces their number.

Line and star artefacts caused by strongly absorbing particles within the specimen are rare. Hence these artefacts do not influence the applicability of the snake algorithm.

Besides the artefacts, noise increases the problems in the analysis of tomograms. Fig. 3 shows a broadening of the air and PMMA peaks with minor overlap. The noise is the result of the photon statistics. It is possible to reduce the noise increasing the exposure time. The benefit, however, becomes smaller and smaller. Even more important are restrictions from the camera chip, which only allows counting until 16 k. Therefore, a significant level of noise is even present for homogeneous materials. Sophisticated algorithms have to be applied in order to extract the required information.

Elastically deformable contour models (snakes) – 1D elastic structure

The non-rigid shape models start from an initialization of an approximate contour, which is usually a rough estimate. Subsequently, the contour is automatically adjusted to the image structures. A regularization is required to avoid any over-fitting during the automatic adjustment, especially important when the images are noisy. In order to extract the crack out of a 2D image, one can use the physical analogy of a rubber band, which is moved under the influence of two forces: first, the image force F_i that pushes the band towards the crack, and second, the elastic forces F_d of the band that avoid too strong expansions and bending, therefore preventing the over-fitting to low-scale noisy structures. The simple linear elastic behaviour is sufficient for the deformable contour models. The difficulty lies in the selection of the arc length s dependent parameters, i.e. tension $\alpha(s)$, rigidity $\beta(s)$, damping $\gamma(s)$, and mass $\mu(s)$ of the snake. It should be noted that the target is a reasonable local minimum and not the global minimum, because the rubber band has the tendency to shrink, and zero energy

would be reached by shrinking the band to any single point. Another problem to be solved is the appropriate choice of the boundary conditions. Since we can accurately determine the crack at the surface, it is reasonable to fix the band at the exit of the crack, i.e. (x_1,y_1) and (x_2,y_2). The problem can be formulated for a rubber band in 2D space using the energy-based description, depending on the image attractors by means of the related potential field $P(x,y)$.

$$E_I(\vec{x}) = -\iint_{x,y} P(x,y)dxdy$$

$P(x,y)$ is only a function of the image, but there is no unique choice. Following the usual way, the magnitude of the image gradient is applied, here.

The deformation energy E_d, which represents the resistance of the rubber band against bending and stretching, enforces the smoothness of the band. The two linear contributions are the tangential stretching, i.e. the first derivative of s, and the bending, i.e. the second derivative of s.

$$E_D(\vec{x}) = \frac{1}{2}\int_s \left(\alpha(s)\left|\frac{\partial \vec{x}}{\partial s}\right|^2 + \beta(s)\left|\frac{\partial^2 \vec{x}}{\partial s^2}\right|\right)ds$$

, whereby $\vec{x}(s,t) = (x(s,t), y(s,t))$ with t being the time.

The total energy on the band (snake) to be optimized deforming the snake in time is therefore:

$$E(\vec{x}(s,t)) = E_D(\vec{x}(s,t)) + E_I(\vec{x}(s,t)).$$

Often it is necessary to add further energy terms, which is also needed to give the band the physically meaningful behaviour.[5] First, the kinetic energy E_k is introduced:

$$E_k = \frac{1}{2}\int_s \mu(s)\left|\frac{\partial \vec{x}(s,t)}{\partial t}\right|^2 ds.$$

Second, the friction or damping energy E_F is necessary to address the energy dissipation, e.g. modelled through the Rayleigh functional:

$$E_F(\vec{x}) = \frac{1}{2}\int_s \gamma(s)\left|x_t\right|^2 ds$$

Damping related to the energy dissipation does not only lead to the realistic rubber band (snake) behaviour, but especially improves the condition of the stiffness matrix through the diagonal term. Over-damping, however, is undesirable because the snake is glued and does not allow moving.

The snake motion is calculated minimizing the following integral:

$$\int_s \left(E(\vec{x}) + E_k(\vec{x}) + E_F(x_t)\right)ds \rightarrow \min$$

For the numeric solution, we used finite differences and the boundary conditions mentioned above. Smoother image potentials, which simplify the calculation, can be created implementing appropriate filters.

If the tomogram is not well prepared for the snake algorithm, i.e. without the removal of the numerous ring-like artefacts, the image potential is not strong enough to give rise to satisfactory results. Fig. 4 (a) shows that the snake fits the crack well if the snake is in the direct (about 20 to 30 μm) neighbourhood of the crack. If the starting location is not close enough and noisy structure and artefacts are present, the algorithm does not converge towards a reasonable result. One cannot really find any improvement between iteration step 150 and 300. The variation of the snake parameter does not yield significantly better results. Hence, for noisy structures rich of artefacts the model has to be further improved.

It is known that additional energy terms can globally influence the snake behaviour in a positive manner. Here, we have introduced a kind of gravitation, which forces the snake to move into a predefined direction, namely towards the crack. After removal of the ring-like artefacts and applying the additional force, the snake automatically detects the crack in the 2D image within only some 10 iteration steps, as shown by the image sequence in Fig. 4 (b).

Elastically deformable surfaces

The basic idea of the 1D rubber band can be generalized to 2D membranes to detect the crack morphology. One of the simplest solutions is to build the membrane out of a finite number of equivalent elastic bands in parallel fashion. Such a membrane once obtained can be used to make visible the crack and to quantify its features.

In order to demonstrate that the snake algorithm provides better results than the state-of-the-art estimates we have implemented two approaches for our specimens: the mass centre point method and the minimal intensity method. The minimal intensity approach transforms the 3D data set into a 3D height field using a ray tracer. The visualization of the crack using the minimal intensity approach can be also realized by the ray casting.[21] The simple initializations, including ray casting, are not enough to obtain the desired crack morphology in a quantitative manner, although meaningful representations of restricted areas of rather homogeneous specimens are reported.[2]

Following the mass centre point method, we have searched for neighbouring ‘air’ voxels to be labelled. The mass centre points of the identified clusters should allow generating the approximated crack surface. The size of the identified clusters should be restricted to suppress the area outside the PMMA specimen and, more important, to avoid the incorporation of the

numerous artefacts. In order to avoid the incorporation of clusters, which are generated because of noise, a minimal cluster volume should be also set. Using a minimal cluster volume of 20 voxels and a maximal volume of 100 voxels we have reduced the number of points from 3127 to 2005. Although this approach yields interpolation values of the crack, their density is inappropriate to visualize the characteristic crack features.

Better results are obtained by the minimal intensity method, although several steps using conventional software were necessary. In the first step, we have produced the height field and the intensity image, respectively, which already provide an idea of the crack morphology.[22] In order to improve the visualization, the grey values below the threshold (cp. Fig. 3) are set to zero. Of course, the results are much better after the removal of ring-like artefacts. Noise is reduced by the application of a median filter, or even better by the use of the 'dust and scratch removal' filter of Adobe Photoshop. Finally, POV Ray was chosen to visualize the height field, as shown in the upper part of Fig. 5. In the central part, many fine details are visible. Hence, this approach leads to images, which can be used, besides the SEM images, for the validation of the snakes approach. Please note, however, that additional artefacts occur in the marginal zones. The estimate is only locally helpful and the artefacts, especially the strong ring-like artefacts, are pronounced.

The snake approach of the elastic band is line-wise generalized to the elastic membrane. Although the additional force in y-direction is very supportive, the selection of the parameters is still time-consuming. One of the results is shown in Fig. 5 (b), where the tension is set to 26, the rigidity to 9, the mass of the snake to 30, and the damping to 1.[22] We have realized that the choice of the threshold is important for the success of our approach. During the iterations, we have observed the convergence of the snake in 3 planes perpendicular to the crack. This enabled us to decide on the termination of the programme and to search for the most appropriate snake parameters. The image in Fig. 5 (b) clearly demonstrates that the application of the snake algorithm considerably reduces the artefacts visible in the minimal intensity method images but conserves the crack features of micrometer size.

Discussion and conclusions

The application of the snake algorithm using an elastic membrane to be adapted to the SRμCT data allows the non-destructive visualization of the crack morphology with micrometer resolution. Because the data are acquired non-destructively without any use of contrast agent, the crack propagation can be followed in time. The limitation is the amount of data generated,

i.e. several gigabyte per step and the time-consuming data analysis. We expect, however, that once the appropriate procedures and parameters are identified, the data analysis becomes straightforward. As shown in Fig. 6, SEM images show much more details with respect to SRμCT data due to the higher lateral spatial resolution. Therefore, the combination of SRμCT and sophisticated 3D data analysis will not replace the SEM images of cracks, which are obtained after the specimen is fractured, but will be rather complementary. Please note that the quantification of the crack morphology by the use of SEM images[23] is a very expensive task, too, and the membrane, which contains the features with equidistant resolution in the three orthogonal directions on the micrometer scale, can help to calibrate the approximations calculated from the SEM images.

For the homogeneous specimen such as PMMA, the approach works in an automatic way. For dental composites, however, the estimate to initialize the snakes has to be found within restricted volumes mainly manually. Another limitation of our approach is that multiple, branching cracks can only be handled in sub-volumes, where just one single crack is present.

Concerning morphology representation the approach has the problem to round the edges of the crack. In order to obtain the desired replica of the crack the snake parameters have to be carefully selected.

It should be noted that the synchrotron radiation source we used belongs to the second generation. Therefore, the prominent edge enhancement at the crack surfaces ('Schlieren'-type) due to the coherence of the X-rays from the third-generation sources[3] are mainly suppressed. Because of the restricted numbers of photons, however, the noise level might be higher for the tomography using second-generation synchrotron radiation sources. Toda et al.[2] pointed out that noise and artefacts, which are directly reflected in the quantitative results such as crack-opening, are not specifically described in the literature. Consequently, the presented quantitative data are somehow questionable, especially if sub-voxel interpolation is integrated.

Intensity-based segmentation algorithms rely on the appropriate choice of the threshold. The rather simple estimates work only for very specific cases. The choice of Lee et al.[24] is too simple, since their histogram presented does not exhibit 2 peaks of identical amplitude and width. This might be also the reason, why they subsequently presented a different approach.[1] The sensitivity analysis, as given by Toda et al.[2] does not yield the optimal choice for the threshold, but shows that the feature detection and its robust measurement are relatively independent on the thresholding conditions. In a previous paper,[19] we have demonstrated that the absorption histograms of tomograms generated at the second-generation synchrotron have

a perfect Gaussian distribution and allow determining the threshold from the crossing point of the two Gaussians, if two distinct peaks are present. The broadening of the peaks is often correlated with the noise, which complicates the visualization of the features of interest (here the crack) just using the intensity-based segmentation procedures. Especially for medical imaging, knowledge-based algorithms are developed. Since we assume that the crack forms a 2D object with well-defined boundary conditions and without any bifurcation in the region of interest, our approach belongs to the knowledge-based procedures.

Despite the numerous difficulties and the rather expensive data preparation for the application of the snakes to the fatigue crack, the combination of the non-destructive 3D visualization by SRμCT and highly sophisticated computer vision methods using elastically deformable contour models enables the accurate determination of the fatigue behaviour of the material to be characterized and optimized.

Acknowledgements

The authors are grateful to Gábor Szekely, who provided the idea to apply the snake algorithm to visualize the crack, and acknowledge the support of Philipp Thurner during the data acquisition.

References

[1] A. Guvenilir, T. M. Breunig, J. H. Kinney, et al., Acta Metallurgica **45**, 1977 (1997).
[2] H. Toda, I. Sinclair, J.-Y. Buffiere, et al., Phil. Mag. **83**, 2429 (2003).
[3] A. Steuwer, L. Edwards, S. Pratihar, et al., Nucl. Instrum. Meth. in Phys. Res. **B 246**, 217 (2006).
[4] M. Kass, A. Witkin, and D. Terzopoulos, Intern. J. Comp. Vision **1**, 321 (1988).
[5] W. Neuenschwander, *Elastic deformable contour and surface models for 2-D and 3-D image segmentation* (Hartung-Gorre Verlag, Konstanz, Germany, 1996).
[6] C. H. Lloyd and J. N. Anderson, J. Oral Rehab. **7**, 155 (1980).
[7] G. D. Stafford, R. Huggett, and B. E. Causton, J. Biomed. Mater. Res. **14**, 359 (1980).
[8] K. Kvam, Biomaterials **13**, 101 (1992).
[9] R. M. V. Pidaparti, W. A. Boehmer, and M. W. Beatty, Eng. Fracture Mech. **45**, 51 (1993).
[10] L. E. Tam and R. M. Pillar, J. Dent. Res. **72**, 953 (1993).
[11] L. M. Barker, Eng. Fracture Mech. **9**, 361 (1977).
[12] R. M. Pillar, D. C. Smith, and B. Maric, J. Dent. Res. **65**, 1308 (1986).
[13] R. M. Pillar, R. Vowles, and D. A. Williams, J. Biomed. Mater. Res. **21**, 145 (1987).
[14] N. D. Ruse, T. Troczynski, M. I. MacEntee, et al., J. Biomed. Mater. Res. **31**, 457 (1995).
[15] L. Grodzins, Nucl. Instrum. Meth. **206**, 541 (1983).
[16] B. Müller, P. Thurner, F. Beckmann, et al., in *Developments of X-ray tomography III*, edited by U. Bonse (SPIE, San Diego, 2001), Vol. 4503, p. 178.

[17] F. Beckmann, in *Developments in X-ray Tomography III*, edited by U. Bonse (SPIE - The International Society for Optical Engineering, San Diego, USA, 2001), Vol. 4503, p. 34.
[18] A. C. Kak and M. Slaney, *Principles of Computerized Tomographic Imaging* (Society of Industrial and Applied Mathematics, 2001).
[19] B. Müller, F. Beckmann, M. Huser, et al., Biomol. Eng. **19**, 73 (2002).
[20] J. Sijbers and A. Postnov, Phys. Med. Biol. **49**, N247 (2004).
[21] S. D. Roth, Comp. Graphics Image Processing **18**, 109 (1982).
[22] F. Pfrunder and L. Chiocca, in *Computer Vision Lab, Electrical Engineering and Information Technology* (ETH Zurich, Zürich, Switzerland, 2004).
[23] E. Ponz, J. L. Ladaga, and R. D. Bonetto, Microscopy and Microanalysis **12**, 170 (2006).
[24] S.-B. Lee, S. R. Stock, M. D. Butts, et al., J. Mater. Res. **13**, 1209 (1998).

Figure captions

1. The photograph of the fatigue crack in PMMA after destruction of the specimen is shown in the upper part. On the left hand side the specimen is gold coated. This is used for secondary electron microscopy represented in the lower part. Here, one can clearly identify the initiation point (left corner), the different characteristic zones of the fatigue crack and, opposite to the initiation point, the trapeziform surface of the break, which was generated after SRμCT data acquisition.
2. The acquired tomogram has a height of 3 mm. Since the crack in the PMMA specimen is located within a height of about 0.4 mm, the amount of data can be reduced to the region of interest, i.e. the triangular specimen's cross section and a stack of 76 slices each 5 μm thick, which is a reduction of more than one order of magnitude (to 113 MB). On the left, the location of the crack is made visible using slices 50 μm thick. The individual slices, however, do not provide the crack morphology, which would allow drawing conclusions on crack origin and formation.
3. Because the PMMA specimen is homogeneous, the absorption histogram just exhibits two peaks (material and air) and a certain amount of partial volume effects between them. The peaks are well separated. Consequently, the threshold for intensity-based segmentation can be set to the crossing point of both Gaussians.
4. In general, the snake algorithm is applied to lines in a two-dimensional manner as demonstrated here. In (a) the grey-values of the pixels give rise to a potential, which forces the snake towards the crack. Obviously, this potential is not strong enough to identify the crack. Therefore, a driving force is added. Together with further improvements such as artefact reduction, this approach even allows the choice of less suitable starting values but

to guarantee the unique identification of the crack in a two dimensional dataset. The number of iteration steps is indicated.

5. For homogeneous materials simple approaches such as visualizing the minimal intensity voxels in the projection plane enables the extraction of many details (cp. (a)). The snake algorithm, however, results in rather smooth images with only very few artefacts, because the artefacts located sufficiently far from the crack are eliminated.
6. The snake algorithm applied to SRμCT data only enables the visualization of features with sizes larger than the spatial resolution, i.e. here 9 μm. SEM yields, therefore, much more details. Because SEM images of the crack surface can only be obtained after the specimen failure, both methods are complementary. The crack formation, followed by SRμCT, can be subsequently validated by the use of SEM images.

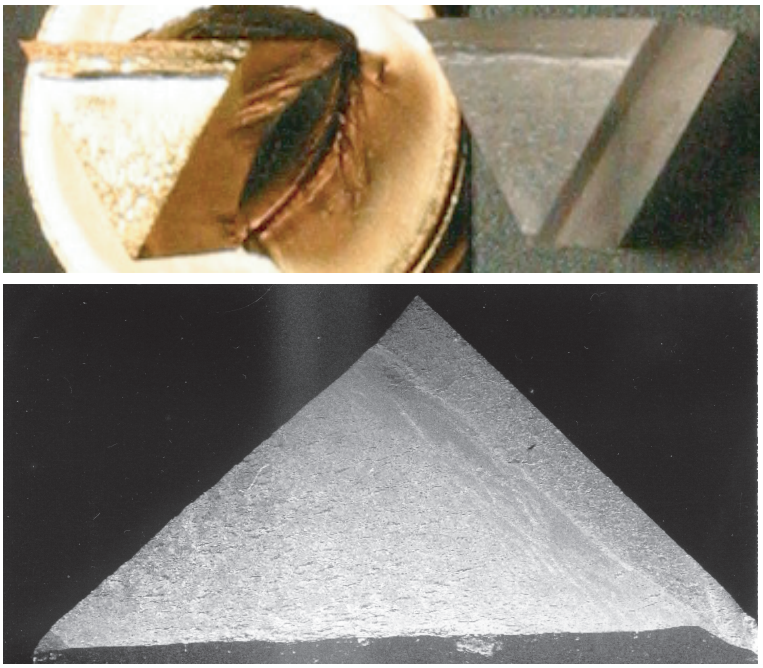

Figure 1 (B. Müller et al.)

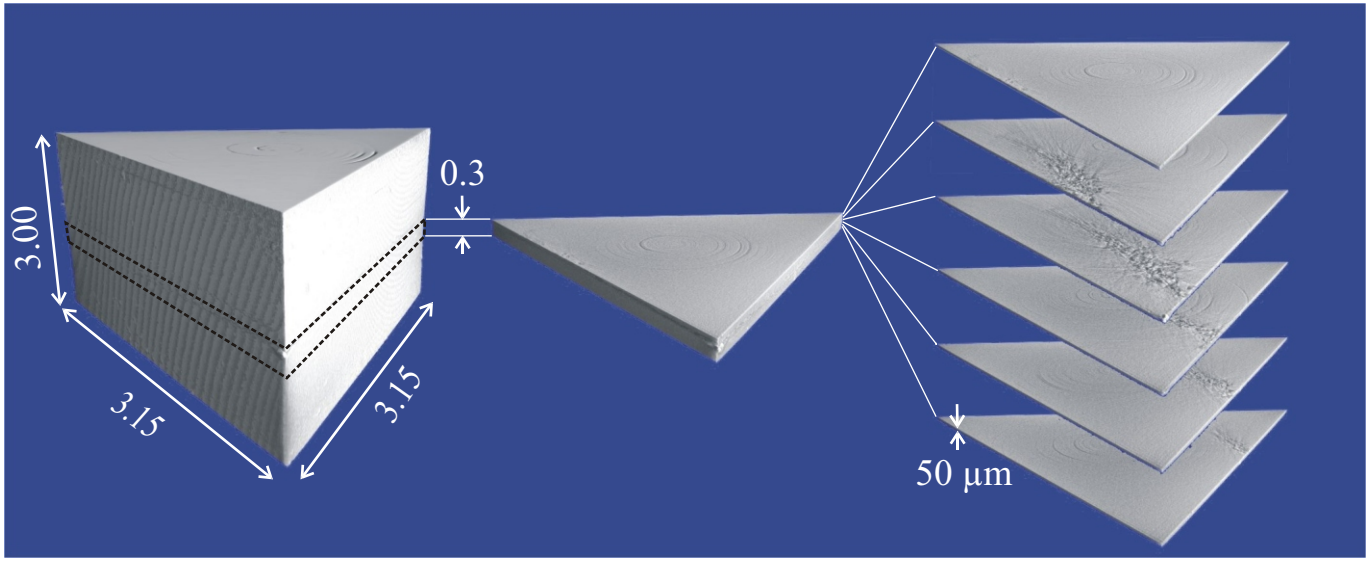

Figure 2 (B. Müller et al.)

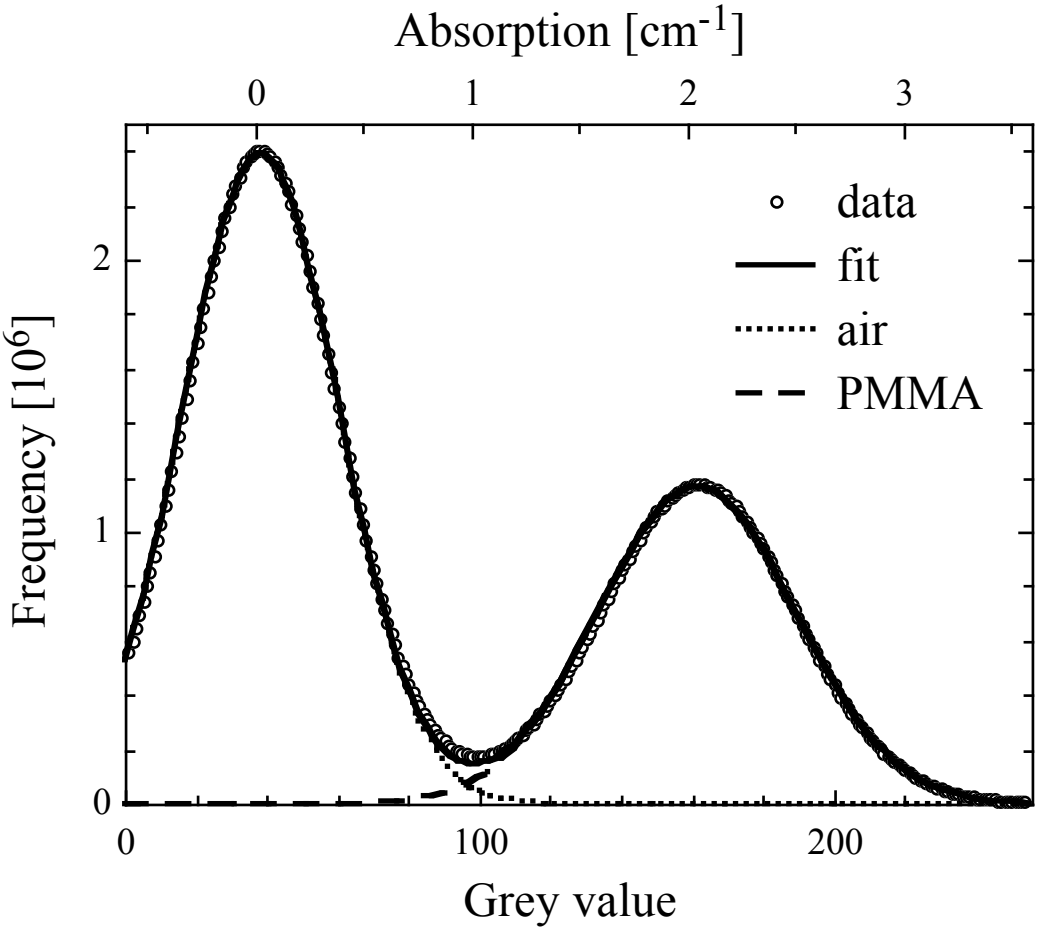

Figure 3 (B. Müller et al.)

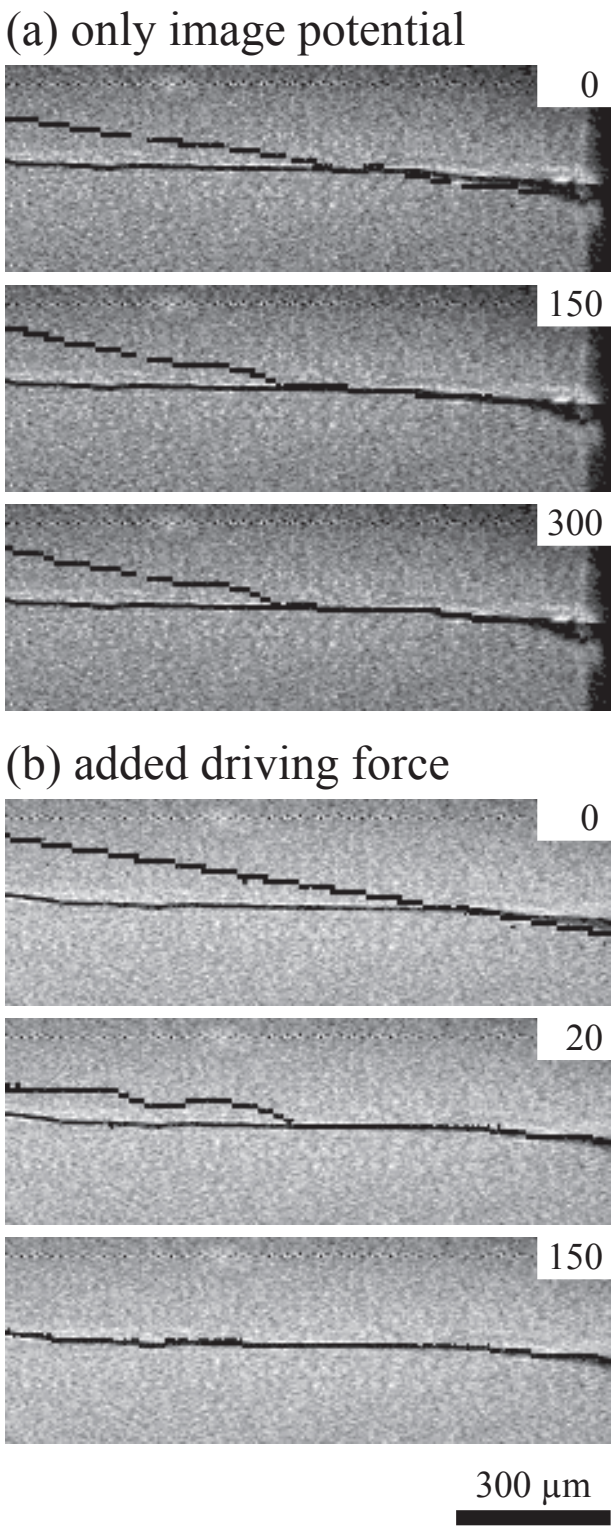

Figure 4 (B. Müller et al.)

(a) minimal intensity

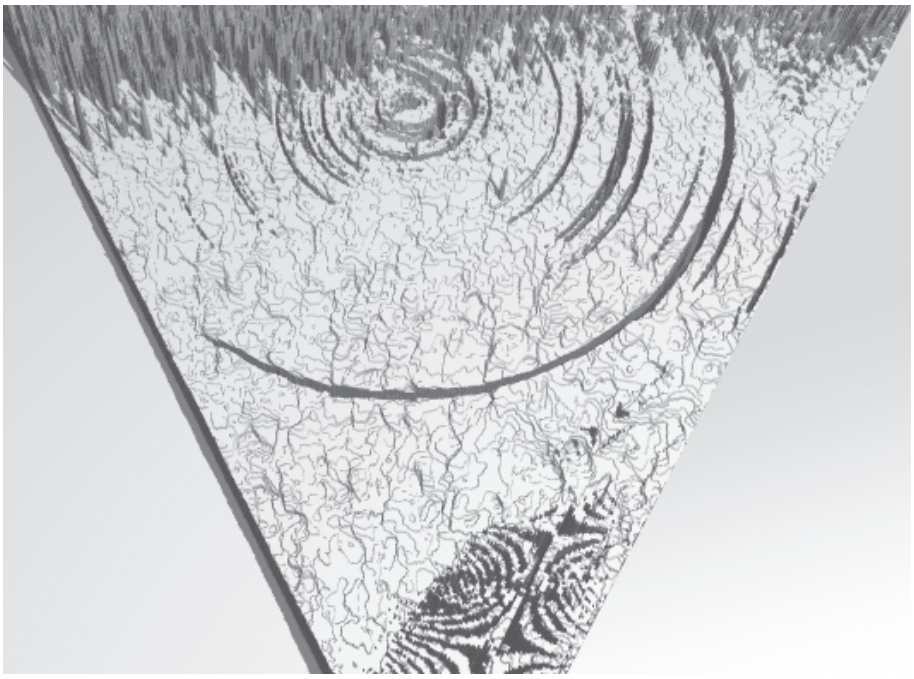

(b) snakes

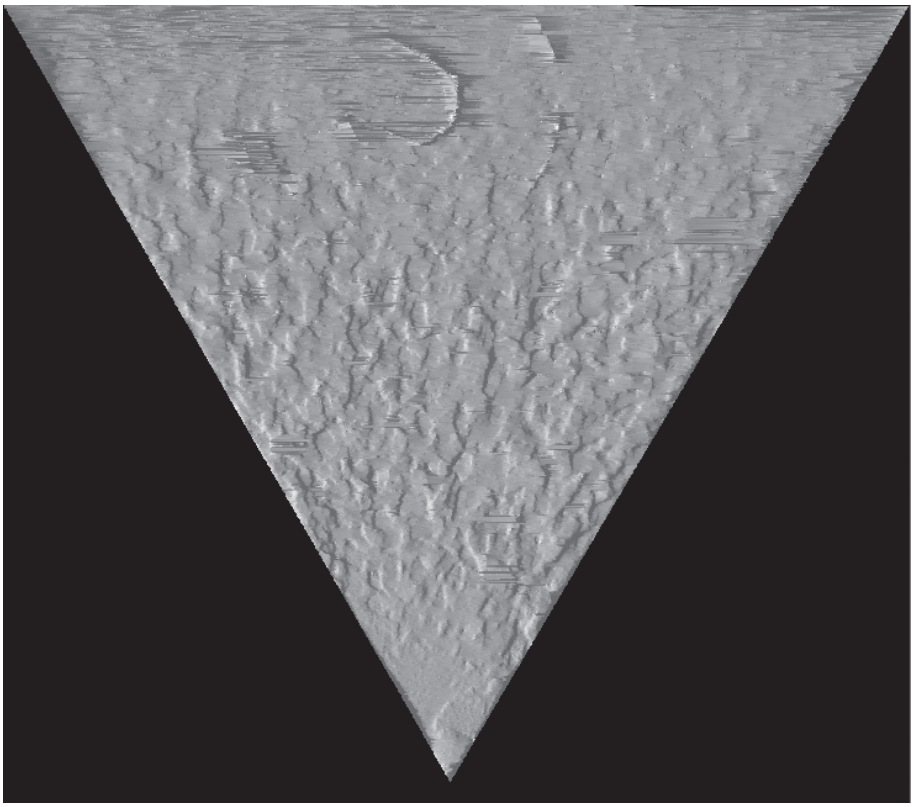

Figure 5 (B. Müller et al.)

(a) SRμCT and snakes

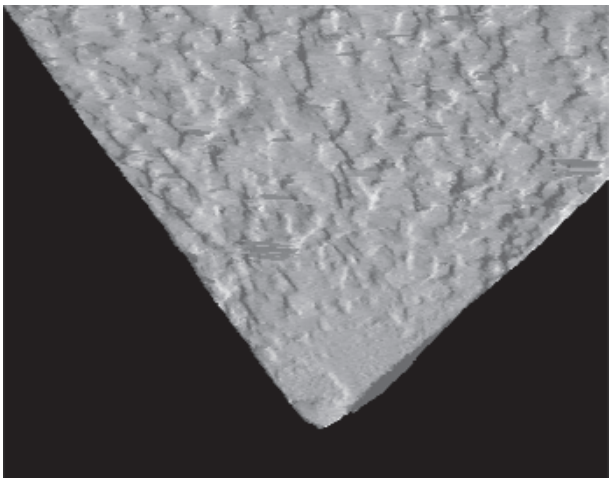

(b) electron microscopy

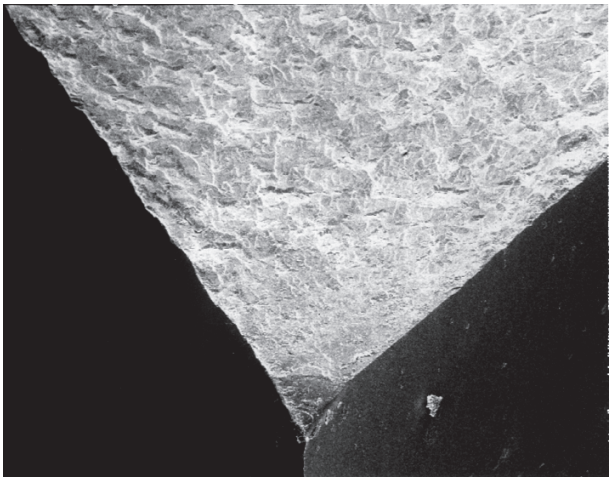

Figure 6 (B. Müller et al.)